Nanoscale Advances

ROYAL SOCIETY OF CHEMISTRY

PAPER

View Article Online
View Journal | View Issue

Cite this: *Nanoscale Adv.*, 2021, **3**, 3554

Mitigation of vacancy with ammonium salt-trapped ZIF-8 capsules for stable perovskite solar cells through simultaneous compensation and loss inhibition†

Chi Li,‡[a] Shanshan Guo,‡[a] Jingan Chen,[a] Zhibin Cheng,[a] Mengqi Zhu,[a] Jindan Zhang,*[ab] Shengchang Xiang[ab] and Zhangjing Zhang*[ab]

Due to the easy loss of ions during synthesis or usage, vacancies in perovskite film are ubiquitous, accelerating the degradation of perovskite materials and seriously hampering the stability of perovskite solar cells (PSCs). Herein, to simultaneously compensate for vacancies and reduce ammonium cation loss, a sustained release strategy was proposed by introducing multi-functional capsules consisting of zeolitic imidazolate framework-8 (ZIF-8) encapsulation agent and ammonium iodide salts as interlayer between the perovskite and hole transport layer. In the capsule interlayer, not only are ammonium iodide salts in ZIF-8 pores released to the perovskite layer, compensating for the vacancies, but the ZIF-8 also prevents the organic component of perovskite from evaporating and isolates the perovskite from moisture. As a consequence, decreased trap density, improved device efficiency, and enhanced stability of PSCs are obtained owing to the successful passivation of defects by the introduced capsules. ZIF-8@FAI shows the highest efficiency of 19.13% and a stabilized PCE over 93% of the initial efficiency at maximum power point for 150 h. This work provides a new strategy to improve efficiency and stability of PSCs based on the large family of porous materials.

Received 7th March 2021
Accepted 19th April 2021

DOI: 10.1039/d1na00173f

rsc.li/nanoscale-advances

Introduction

Perovskite solar cells (PSCs), which are based on organic–inorganic lead halide perovskite absorbers with unique and intriguing optoelectronic properties, have received increasing attention due to their low cost and high power conversion efficiency (PCE).[1–6] Mainly benefiting from the great efforts on engineering the device structure, solvent, composition, additive, and interface, the PCE of PSCs has been strikingly enhanced from the original 3.8% to the presently certified 25.5% within only several years.[7–15] However, in state-of-the-art PSCs, there exists significant non-radiative loss in the perovskite absorber, mainly originating from ionic defect states such as methylamine (MA^+) or formamidine (FA^+) ion vacancies, limiting further improvement of the device performance.[16–18] Simultaneously, those vacancies are believed to be a target for attacks from the external environment, such as moisture, heat or light, resulting in perovskite degradation and device instability.[19–22] To suppress the formation of such vacancies, one efficient way is to use excess halogenated MA/FA during or after the perovskite annealing process.[23–28] The evaporation and loss of organic components persist during usage or under the attack of moisture, limiting the durability of the perovskite. Thus, to passivate the cation vacancies and further mitigate evaporation of organic components, many recent studies developed a two-dimensional (2D) perovskite on a three-dimensional perovskite surface by introducing a small amount of hardly volatile organic ammonium salts with a larger molecule.[9,29–31] Unfortunately, the lack of effective ways to accurately control the *n*-value in the 2D phase hinders surface conductivity, harms the reproducibility of device efficiency, and results in more complicated carrier transport in the perovskite. Thereby, a convenient strategy to effectively maintain organic ammonium content for cation vacancy suppression is crucial and urgent.

Inspired by the interface construction in metal corrosion inhibition science, we propose a sustained-release strategy to realize controllable supplementation and loss inhibition (under thermal or moisture condition) of organic ammonium by introducing multifunctional capsules encapsulating

[a]*College of Chemistry and Materials Science, Fujian Provincial Key Laboratory of Polymer Materials, Fujian Normal University, 32 Shangsan Road, Fuzhou 350007, China. E-mail: zhangjindan@fjnu.edu.cn; zzhang@fjnu.edu.cn*

[b]*State Key Laboratory of Structural Chemistry, Fujian Institute of Research on the Structure of Matter, Chinese Academy of Sciences, Fuzhou, Fujian 350002, PR China*

† Electronic supplementary information (ESI) available: Additional SEM, pore size distribution, TGA curves, EDS mapping, UV-vis absorption, *J–V* curves, resistance spectra and values, photovoltaics parameters, stability test. See DOI: 10.1039/d1na00173f

‡ Chi Li and Shanshan Guo contributed equally to this work.

ammonium salt to the perovskite and hole transport material (HTM) interface. With the help of capsule encapsulation, evaporation of the ammonium salt inside capsules is suppressed, effectively overcoming the disadvantages of the "excess methylamine" approach and, thus, avoiding the problems induced by the large ammonium molecules. To develop these capsules, the encapsulation agents should possess a porous structure with suitable pore size to contain the ammonium salts and release them in suitable conditions; meanwhile, it should be hydrophobic to protect the perovskite layer against moisture. In this regard, metal–organic frameworks (MOFs) would be desirable materials due to the characteristic structural and componential controllability,[32–36] hydrophobic property[37–40] and chemical stability.[41–45]

Herein, by harnessing its superior perovskite affinity[34] and hydrophobicity, zeolitic imidazolate framework-8 (ZIF-8) was utilized as an encapsulation agent to generate a sustained-release capsule containing ammonium iodide (Fig. 1a). After introduction into PSCs as an interlayer between perovskite and HTM (Fig. 1b), the sustained-release capsules not only effectively passivated the generated vacancies by releasing the trapped ammonium iodide, driven by concentration gradient in the defect area, but also inhibited the loss of ammonium ion by blocking the ammonium iodide salt in perovskite against evaporation. Furthermore, the hydrophobic ZIF-8 agent protected the perovskite from environmental water attack. Therefore, capsules consisting of ZIF-8 and MAI/FAI are confirmed effective to passivate perovskite defects, block MA evaporation and isolate moisture, simultaneously. As a result, the device based on ZIF-8@MAI or ZIF-8@FAI shows significantly improved PCE and stability. Among these, ZIF-8@FAI shows a PCE of 19.13% and a stabilized PCE, maintaining over 93% of the initial PCE at maximum power point for 150 h.

Experimental

Materials and methods

All reagents and solvents used were commercially available without further purification. The surface morphologies and element distributions of the perovskite films were investigated using field emission scanning electron microscopy (SEM) and energy dispersive spectroscopy (EDS) analysis (JSM-7500F, Japan). X-ray diffraction (XRD) was carried out with a PANalytical X'Pert3 powder diffractometer equipped with a Cu sealed tube (λ = 1.541874 Å) at 40 kV and 40 mA over the 2θ range of 5°–50°. The N_2 adsorption/desorption isotherms were obtained at 77 K on a Micromeritics ASAP 2020 HD88 surface area analyzer. X-ray photoelectron spectroscopy (XPS) data were obtained using an ESCALAB Xi$^+$ XPS system (Thermo Fisher Scientific) with Al Kα X-ray radiation (1486.6 eV). UV-vis spectra were obtained from a Lambda 950 spectrophotometer. Water contact angle was measured using a DSA25 contact angle instrument. Photoluminescence (PL) was measured with an Edinburgh Instruments Ltd. FLS 980 spectrometer. Thermal analysis was carried out on a METTLER TGA/SDTA 851 thermal analyzer from 30 to 800 °C at a heating rate of 2 °C min^{-1} under N_2 flow. The current–voltage (J–V) curves were measured under illumination at AM 1.5 G (100 mW cm^2) using a solar simulator

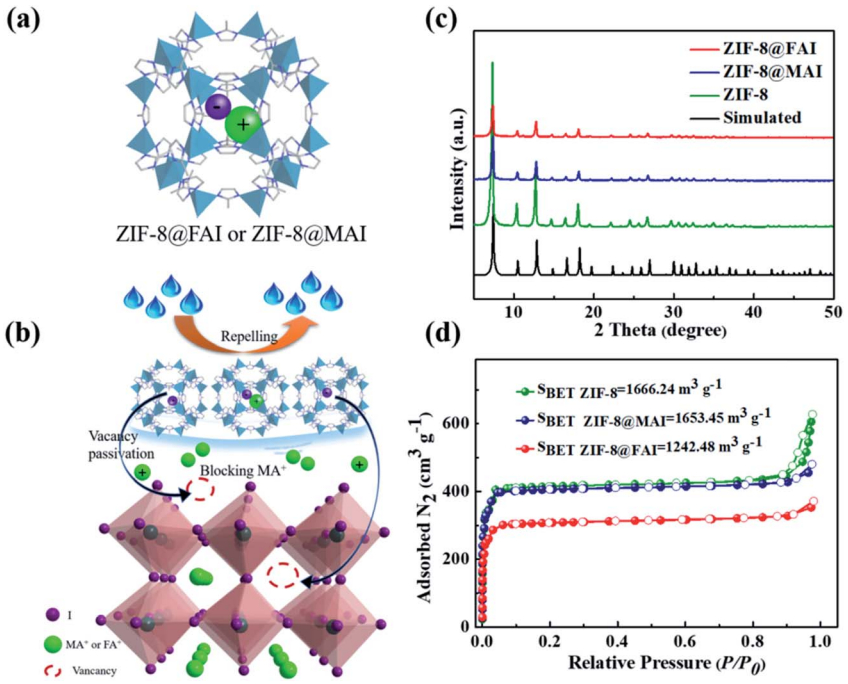

Fig. 1 (a) Chemical structure of ZIF-8@ammonium iodide salts. (b) Schematic illustration of effect of ZIF-8@ammonium iodide capsule on perovskite. The ammonium iodide salts in ZIF-8 diffuse to perovskite layer and occupy the organic cation and halide vacancies. Meanwhile, the ZIF-8 framework isolates the perovskite from moisture and bars the organic component of perovskite from evaporating. (c) XRD patterns and (d) nitrogen adsorption (solid circle)-desorption (empty circle) isotherms at 77 K of ZIF-8, ZIF-8@MAI and ZIF-8@FAI.

(Newport, Oriel Class A, 91195 A, equipped with a 300 W xenon lamp) and a source meter (Keithley 2420). The maximum power point (MPP) tracking was measured by monitoring photocurrent with a bias voltage at the maximum power point. Electrochemical impedance spectroscopy (EIS) spectra were recorded with a Zahner Pro2 electrochemical work station from 1 Hz to 10^5 Hz at 0.9 V in the dark, then fitted using the Z-view software. The photo-to-current conversion efficiency (IPCE) spectra were collected using a Newport IPCE measurement system, and the light intensity was adjusted by an NREL-calibrated Si solar cell. The active area of solar cells was 0.09 cm^2. The trap density measurement was performed with device structure FTO/perovskite/MoO_3/Ag. The trap density was estimated according to the equation:

$$n_t = \frac{2\varepsilon_r\varepsilon_0 V_{TFL}}{eL^2}$$

where n_t is the trap density, ε_r is the dielectric constant of the polymer, ε_0 is vacuum permittivity, L is thickness of the active layer, and e is the elementary charge. V_{TFL} is obtained by fitting the dark I–V data with the equation.

Syntheses of ZIF-8, ZIF-8@MAI and ZIF-8@FAI

Zinc nitrate hexahydrate ($Zn(NO_3)_2\cdot 6H_2O$, 73.44 mg) was dissolved in 25 mL methanol as solution A, and 2-methylimidazole (810.6 mg) was dissolved in 50 mL methanol as solution B. Then, solution B was slowly poured into solution A with stirring. After stirring for 1 h, the precipitate was collected by centrifugation, washed with methanol three times and dried at room temperature.[46] Then, the obtained ZIF-8 powder was added into a saturated MAI or FAI ethanol solution with continuous stirring for 24 hours. The resulting ZIF-8@MAI and ZIF-8@FAI capsule powders were captured by filtration, washed with ethanol, and dried in air.

Device fabrication

PSCs were prepared with a FTO/TiO_2/$CH_3NH_3PbI_3$/HTM/Ag structure. Fluorine-doped tin oxide (FTO, 1.5 × 1.5 cm^2) glass (15 Ω m^{-2} square, NSG, Japan) substrates were ultrasonically washed with deionized water in an ultrasonic bath, followed by acetone and ethanol for 20 min, respectively. Then, the compact titanium dioxide (bl-TiO_2) film was deposited *via* spin-coating titanium(IV) isopropanol (112 μL), in 2.5 mL *n*-butanol solution, at 2800 rpm for 20 s. After annealing at 500 °C for 30 min in air, a TiO_2 paste (Dyesol DSL 30NR-D) in isopropanol (1 : 20, mass ratio) was spin-coated on the substrate at 4000 rpm for 30 s, followed by annealing at 550 °C for 30 min. The perovskite solution was prepared by dissolving 159 mg CH_3NH_3I and 461 mg PbI_2 in 1 mL mixed solvent of DMF and DMSO (volume ratio 4 : 1). Then, the solution was coated onto the mp-TiO_2/bl-TiO_2/FTO substrate by two consecutive spin-coating steps, at 1000 and 6000 rpm for 10 s and 20 s, respectively. During the second spin-coating step, 150 μL chlorobenzene was dropped onto the substrate after 5 s. The intermediate phase substrate was then put on a heating plate at 110 °C for 10 min. Then, for surface treatment samples, ZIF-8, ZIF-8@MAI, or ZIF-8@FAI-solution in isopropanol at different concentrations (0.5 mg mL^{-1}, 1 mg mL^{-1}, 2 mg mL^{-1}, 3 mg mL^{-1} and 4 mg mL^{-1}) were spin-coated at 4000 rpm for 20 s, followed by annealing at 100 °C for 2–3 min. The hole transport layer (HTL) films (72.9 mg of Spiro-OMeTAD in 1 mL chlorobenzene with the addition of 17.5 μL of Li-TFSI solution [520 mg in 1 mL acetonitrile] and 29 μL of *t*-BP) were spin-coated at 4000 rpm for 30 s. All procedures were completed in a nitrogen-filled glovebox. Finally, 4 nm MoO_3 and 100 nm silver top electrode was thermally evaporated.

Results and discussion

To develop a multi-functional interlayer between perovskite and HTM with defect passivation and cation/moisture barrier blocking abilities (Fig. 1a and b), ZIF-8@MAI or ZIF-8@FAI capsules were fabricated first. As shown in Fig. 1c, sharp peaks in the XRD spectra of ZIF-8@MAI and ZIF-8@FAI were attributed to the synthetic ZIF-8, which exhibited high crystallinity. To prove MAI or FAI was successfully encapsulated inside the pores of ZIF-8, specific surface area (Fig. 1d and S2a†), TGA (Fig. S2b†), and elemental mapping scan (Fig. S3†) measurements were carried out. As shown in Fig. 1d, the specific surface areas of ZIF-8@MAI and ZIF-8@FAI were relatively lower than the pristine ZIF-8 sample, suggesting the pores of ZIF-8 were occupied by MAI or FAI. The pore distribution showed the main pores of ZIF-8 were partly occupied, and the incomplete occupation could be ascribed to the vacuum extraction process during the specific surface area measurement. Moreover, the encapsulation of MAI or FAI was further confirmed by the weight loss before 100 °C in ZIF-8@MAI or ZIF-8@FAI TGA curve, and also by the iodine distributions in the elemental mapping scan image.

Then, we carried out a series of characterizations of the perovskite films with ZIF-8, ZIF-8@MAI or ZIF-8@FAI layer on their surface. The corresponding samples were named ZIF-8, ZIF-8@MAI and ZIF-8@FAI, respectively, and the perovskite film without any treatment (namely, pristine) was used as control. As shown in Fig. 2a–d, after the incorporation of functional layers, average grain sizes of perovskite films increased to ~250 nm for the ZIF-8 based sample, to ~300 nm for the ZIF-8@MAI sample and to ~420 nm for the ZIF-8@FAI sample, which are about 1.25, 1.5 and 2.1 times that of pristine film (200 nm). Simultaneously, perovskite films with functional layers exhibited more uniform size, without obvious pinholes. The cross-sectional SEM images of devices are shown in Fig. S8.† Results showed that the incorporation of ZIF-8-based capsules induced less grain boundary and increased crystal size in the internal perovskite layer. Moreover, due to the hydrophobicity of ZIF-8, perovskite films with MOF-based functional layers showed larger water contact angles (62.5° for ZIF-8@FAI, 60° for ZIF-8@MAI and 55° for ZIF-8) than pristine film (43.6°), indicating the enhanced hydrophobicity to resist moisture. In the XRD patterns (Fig. 2e), all perovskite films showed perovskite characteristic peaks at 14.2° (110), 24.9° (202), and 19.4° (220). The full width at half-maximum (FWHM) values (Fig. 2f) of the (110) peak from a Gaussian curve fit were

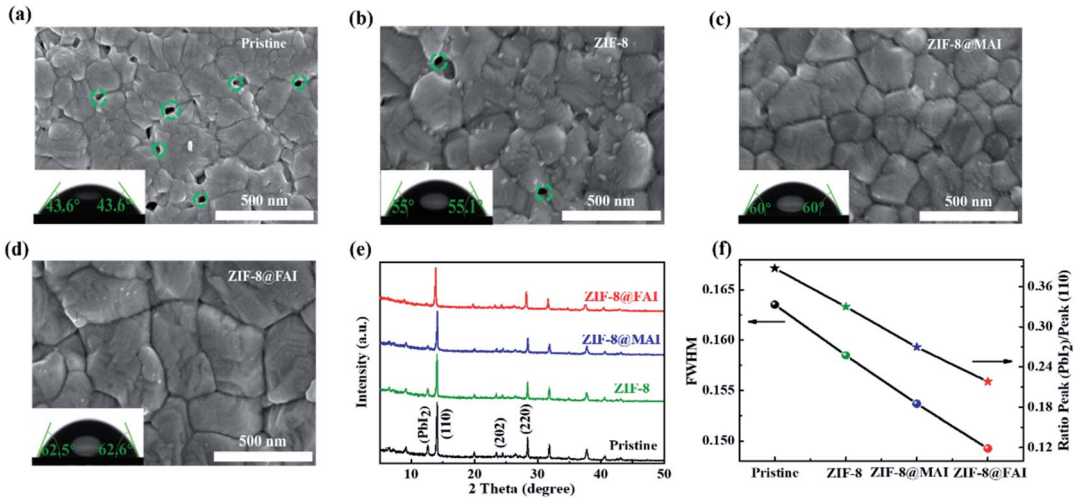

Fig. 2 Top-view SEM images of (a) pristine, (b) ZIF-8, (c) ZIF-8@MAI and (d) ZIF-8@FAI perovskite films. Insets in (a)–(d) are images of water contact angles on the corresponding perovskite films. (e) XRD patterns of perovskite films with and without the MOF-based multi-functional layers. (f) FWHM of the (110) peak and intensity ratio of the PbI_2 peak to (110) peak in XRD.

determined to be 0.1585, 0.1537, and 0.1492 for perovskite films with ZIF-8, ZIF-8@MAI, and ZIF-8@FAI, respectively, which were smaller than the pristine film (0.1635), indicating the increased crystallinity. The disappearance of the PbI_2 peak at 12.8°, evidenced by the decrease of PbI_2 peak/(110) peak (Fig. 2f), also showed the higher crystallinity of MOF-treated samples, in accordance with the SEM images. Notably, the better morphology and crystallinity of ZIF-8@FAI than that of ZIF-8@MAI could be attributed to the incorporation of FA cation, which has stronger reorientation ability and superior Goldschmidt tolerance factor, with minimum distortions in the perovskite lattice.[47] As shown in Fig. S4,† the UV-vis absorption spectra show a slight absorption enhancement over the region from 450 to 760 nm, which can be ascribed to the better crystallization and higher film quality. In further analysis based on the Tauc plots, as shown in Fig. S5,† the bandgaps were calculated to be 1.5685, 1.5635, 1.5634, and 1.5599 eV for pristine, ZIF-8, ZIF-8@MAI and ZIF-8@FAI films, respectively. Results show that there is no noteworthy difference in absorption band edge, suggesting a negligible impact of ZIF-8 capsules on the bulk crystal structure of pristine perovskite.

To evaluate the effects of the ammonium salt-trapping ZIF-8 capsule on device performance, PSCs with a structure of FTO/TiO_2/perovskite/MOF-based functional interlayer/HTM/Ag were fabricated (Fig. 3a and b). The current density–voltage (J–V) curves of the best devices are presented in Fig. 3c, and related photovoltaic parameters are listed in Table 1. The device PCE experienced an improvement from 17.23% to 17.69% after

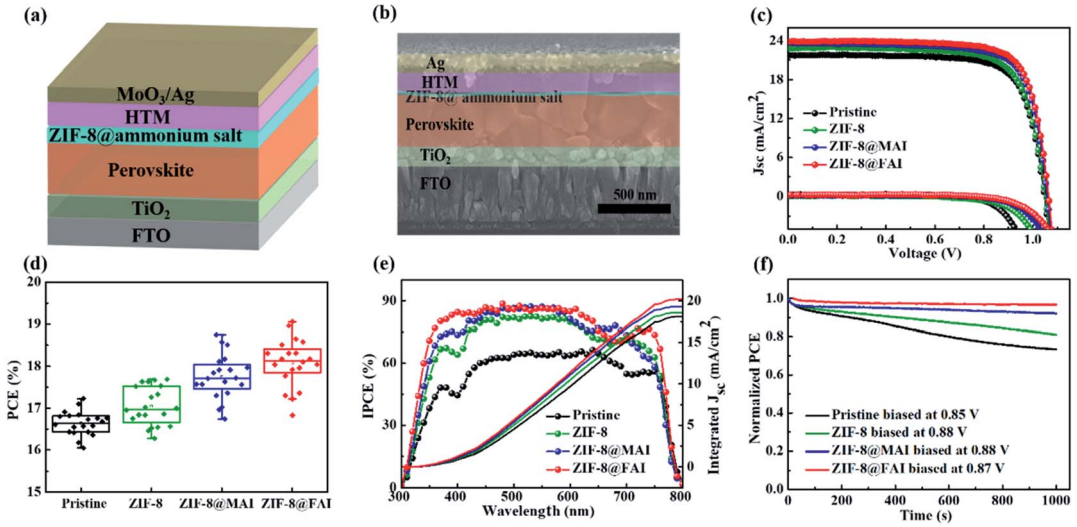

Fig. 3 Photovoltaic characterization of the corresponding PSCs. (a) Schematic representation and (b) SEM images of the cross-sectional view of PSCs; (c) current density–voltage (J–V) curves; (d) PCE histogram based on 20 devices; (e) incident photon-to-current conversion efficiency (IPCE) spectra and integrated J_{sc}; (f) stable output at maximum power point.

Table 1 Photovoltaic parameters for the pristine and ZIF-8, ZIF-8@MAI and ZIF-8@FAI devices

Devices	V_{oc} (V)	J_{sc} (mA cm^{-2})	FF (%)	PCE (%) max (ave)
Pristine	1.047	21.97	74.9	17.23 (16.59)
ZIF-8	1.048	22.46	75.1	17.69 (17.04)
ZIF-8@MAI	1.054	23.78	75.2	18.85 (17.75)
ZIF-8@FAI	1.058	23.93	75.6	19.13 (17.95)

incorporation of the ZIF-8 layer, which could be ascribed to the better morphology of perovskite. The PCE further improved to 18.85% and 19.13% for the ZIF-8@MAI and ZIF-8@FAI-based devices, respectively. The improved open-circuit voltage (V_{oc}) and fill factor (FF) for ZIF-8@MAI and ZIF-8@FAI-based devices resulted from the effective passivation by the functional capsule. The enhancement in current density (J_{sc}) was caused by the stronger light absorption (Fig. S4 and S5†), reduced resistance (Fig. S7†) and high quality of perovskite film. Moreover, the passivation significantly suppressed interfacial recombination, providing a pathway for improved V_{oc}. The *J–V* hysteresis measurements (Fig. S6 and Table S1†) reveal suppressed hysteresis on passivated cells, with hysteresis index (HI) decreasing to 0.213, 0.206, and 0.187 for the ZIF-8, ZIF-8@MAI, and ZIF-8@FAI-based devices, respectively, from an original value of 0.236. The improvement in *J–V* and hysteresis curves indicates a more efficient carrier extraction and reduced recombination. The PCE distribution of 20 individual devices (Fig. 3d and S9†) showed good reproducibility among the devices. Moreover, the dark current appeared at 0.927 V for pristine, and the value increased to 0.998 V, 1.032 V and 1.061 V for the ZIF-8, ZIF-8@MAI and ZIF-8@FAI devices, respectively, indicating that the charge recombination was suppressed. The *J–V* results illuminated that the ZIF-8 capsule-based functional layer, especially the FAI-trapped ZIF-8 capsule, successfully passivated the defects in perovskite. The better performance of ZIF-8@FAI than that of ZIF-8@MAI was ascribed to the better morphology and crystalline degree, as shown in Fig. 2.

The IPCE values and integrated current densities (18.15, 18.61, 19.33, 20.21 mA cm^{-2} for pristine, ZIF-8, ZIF-8@MAI, and ZIF-8@FAI, respectively, Fig. 3e) show trends consistent with those observed from the *J–V* curve, confirming the restrained carrier recombination and the improved perovskite film crystallinity due to passivation of the ZIF-8-based functional layer. Compared to the J_{sc} obtained from *J–V* curves, the integrated current densities were slightly lower, which might be caused by capacitive current owing to *J–V* hysteresis.[48] Fig. 3f shows the curves of normalized PCE as function of illumination time (at AM 1.5, in N_2) while keeping the device at the maximum power point (MPP). The PCE of the pristine device exhibited more than 20% loss within 1000 s, and the PCE remained at 81.05% for the ZIF-8-based PSCs, suggesting their better stability due to the barrier preventing the evaporation of MA cation. Moreover, the value improved to 92.06% and 94.58% for ZIF-8@MAI and ZIF-8@FAI devices in development, indicating that MAI or FAI in the capsule could effectively compensate the MA vacancies in the perovskite.

The space charge limited current (SCLC) was measured to gain further insight into the effect of ZIF-8 capsules on the defect density of perovskite films. As shown in Fig. 4, the trap-filled limit voltage (V_{TFL}) and trap density from SCLC were 0.885 V and 2.26 $\times$ 10^{16} cm^{-3} for pristine, and the corresponding values were 0.837 V and 2.14 $\times$ 10^{16} cm^{-3} for the ZIF-8 sample. The decrease in trap density (n_{trap}) could be assigned to blocking of MA cation evaporation by the ZIF-8 framework. For the ZIF-8@MAI and ZIF-8@FAI samples, the further decreasing n_{trap} (0.794 V and 2.03 $\times$ 10^{16} cm^{-3} for ZIF-8@MAI, 0.751 V and 1.92 $\times$ 10^{16} cm^{-3} for ZIF-8@FAI) illuminated the passivation ability of the trapped ammonium salts in the ZIF-8-based capsule on perovskite.

To confirm the passivation and barrier effects of ZIF-8 and the ammonium salt-trapped ZIF-8 capsule on perovskite film, XPS measurements were conducted. Compared to the pristine perovskite film, both the Pb 4f ($\sim$138 eV and $\sim$143 eV, Fig. 5a) and I 3d ($\sim$619 eV and $\sim$631 eV, Fig. S10†) peaks shifted to lower binding energy for the ZIF-8 sample, indicating the lower oxidation state of lead due to the electron donated by 2-methylimidazole of the ZIF-8 framework. The further shift of XPS peaks to lower binding energy for the ZIF-8@MAI and ZIF-8@FAI samples suggested an interaction between perovskite and ammonium salts. It is known that metallic Pb in perovskite films could become recombination centers and is closely related to iodide vacancies;[49] thus, the disappearance of metallic Pb (140.3 and 135.5 eV) in ZIF-8@MAI and ZIF-8@FAI film demonstrated the passivation of iodine vacancies. In addition, based on these XPS results, the relevant atomic ratios were calculated according to the peak area and sensitive factors and are summarized in Table S3.† The atomic ratios of N/Pb for pristine perovskite only retained 25% of the initial value (decrease from 0.49 to 0.12) after heating at 80 °C in N_2 for 72 h, revealing the serious loss of MA during the heating process. Meanwhile, the value for perovskite with ZIF-8 treatment increased to 68% (from 0.54 to 0.37) due to suppression of MA evaporation by the ZIF-8 framework. The incorporation of MAI and FAI further improved the value to 78% and 83%, respectively, displaying the further passivation of organic vacancies. When considering the I/Pb ratios, similar results were obtained. Pristine perovskite only retained 57% of its initial value (decrease from 3.20 to 1.83) after heating, while the value of perovskite with ZIF-8 treatment increased to 81% (from 3.30 to 2.68). The incorporation of MAI and FAI further improved the value to 85% and 89%, respectively, displaying the further passivation of I vacancies. It should be noted that the reason why the I/Pb ratio is higher than 3 (the theoretical value) is because of the accumulation of I in the surface owing to ion migration. It is notable that the Pb 4f spectra showed stronger interactions with FA cation compared with the MA cation, which led to the higher atomic percentage remaining and better thermal stability of the ZIF-8@FAI sample.

As presented in Fig. 5b, the PL spectra showed a similar trend to XPS, with the PL peak improved after functional layer incorporation, indicating the effective passivation of trap states and reduction of carrier recombination in perovskite film. The PL intensity of perovskite films with functional capsule layers at

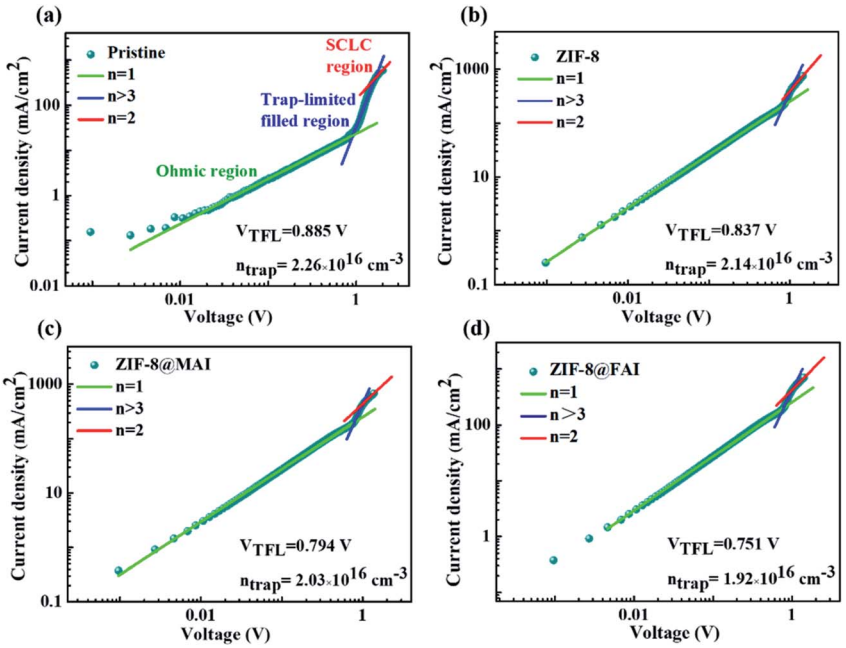

Fig. 4 Dark *I*–*V* curves of devices with the structure FTO/perovskite/MoO_3/Ag for the (a) pristine, (b) ZIF-8, (c) ZIF-8@MAI, and (d) ZIF-8@FAI samples.

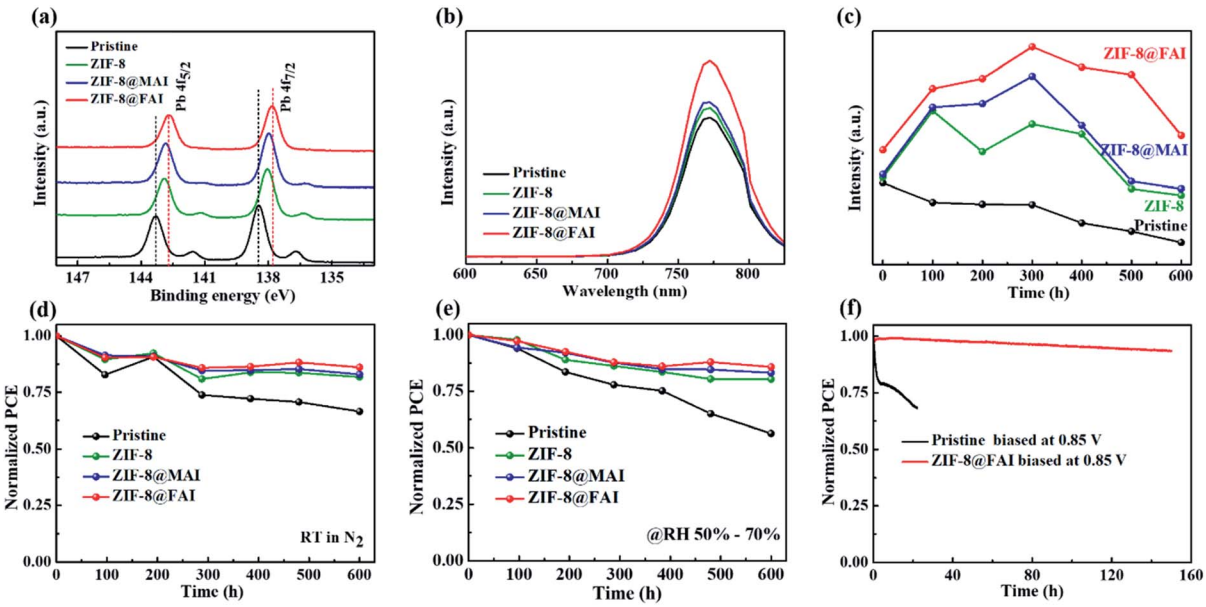

Fig. 5 Stability tests of perovskite films and real devices with and without ZIF-8-based functional layers. (a) Pb4f peaks in XPS spectra. (b) Steady-state photoluminescence (PL) spectra. (c) Evolution of PL intensity at ~772 nm stored at room temperature under natural light for 600 h. (d) and (e) Long-term stability test of unencapsulated perovskite devices stored at room temperature (RT) under natural light in N_2 and in air atmosphere (RT, 50–70% RH). (f) Stable output at maximum power point under a nitrogen environment at room temperature.

~772 nm (Fig. 5c and S11†) was maintained at higher intensity over 600 h compared to the control sample. The increased PL intensity in the first 300 h, as seen in Fig. 5c, could be ascribed to the mitigation of defects induced by the introduction of ZIF-8, which blocks ions and prevents consumption of ions. The dissociated ions in the perovskite layer are subsequently restored to the corresponding vacancies under dark condition to heal the perovskite.[50] For ZIF-8@MAI- or ZIF-8@FAI-based samples, the released MAI or FAI further passivated the vacancies in perovskite, therefore leading to greater improvement in the PL intensity. Time-resolved photoluminescence was monitored, as shown in Fig. S12,† and the related lifetime data are in Table S4.† The lifetime increased from 94.27 (pristine) to 162.01, 258.90 and 272.36 ns by introducing ZIF-8, ZIF-8@MAI

and ZIF-8@FAI devices, respectively. These results demonstrated the restrained non-radiative recombination due to the successful passivation of defects after ZIF-8-based capsule incorporation.

Long-term stability tests of the corresponding unencapsulated PSCs were performed under natural light in nitrogen atmosphere (Fig. 5d), under humidity (50–70 RH%, Fig. 5e) or at 50 °C in N_2 (Fig. S15†). The superior stability of ZIF-8 PSCs compared to pristine PSCs confirmed the hypothesis that the ZIF-8 framework could isolate the perovskite layer from moisture and block the MA cation from evaporating once again. Simultaneously, the device stability improved with MAI and FAI incorporation. The stability of the ZIF-8@FAI device was the best, with 86%, 85.43% and 74.28% of the initial PCE remaining after storage under natural light in nitrogen atmosphere for 600 h, in 50–70 RH% for 600 h, and at 50 °C for 60 h, respectively. Notably, in MPP tests, the ZIF-8@FAI device retained over 93% of its initial PCE value after 150 h, while the pristine device only had ~68% left after 22 h. These results indicate the better operational stability of PSCs with ZIF-8@FAI.

Conclusions

In summary, ZIF-8 capsules encapsulating ammonium iodide salts in their pores (ZIF-8@MAI or ZIF-8@FAI) were used as multi-functional interlayer to passivate perovskite defects, block MA evaporation and isolate moisture. Results showed that the defects were successfully passivated by the ZIF-8 capsules, with trap density decreasing to 1.92×10^{16} cm^{-3} for the best-performing ZIF-8@FAI-based sample. Thus, incorporation of the ZIF-8 capsule layer led to enhanced performance, from 17.23% to 19.13%. In addition, greatly improved thermal and moisture stability was observed. PSCs with ZIF-8@FAI maintained 74.28% of their initial performance after storage at 50 °C for 60 h, as well as over 93% of their initial PCE at maximum power point for 150 h. This work provides a strategy to efficiently improve the efficiency and stability of PSCs based on the large family of porous materials.

Conflicts of interest

There are no conflicts to declare.

Acknowledgements

This work was supported by the National Natural Science Foundation of China (21805039, 52001066, 22005054, 21975044 and 21971038), the Fujian Provincial Department of Science and Technology (2018J07001 and 2019H6012), and the Department of Education (Fujian province) (JT180090).

Notes and references

1 M. M. Lee, J. Teuscher, T. Miyasaka, T. N. Murakami and H. J. Snaith, Efficient hybrid solar cells based on meso-superstructured organometal halide perovskites, *Science*, 2012, **338**, 643.

2 M. Wang, F. Cao, K. Deng and L. Li, Adduct phases induced controlled crystallization for mixed-cation perovskite solar cells with efficiency over 21%, *Nano Energy*, 2019, **63**, 103867.

3 R. Chen, J. Cao, Y. Duan, Y. Hui, T. T. Chuong, D. Ou, F. Han, F. Cheng, X. Huang, B. Wu and N. Zheng, High-efficiency, hysteresis-Less, UV-stable perovskite solar cells with cascade ZnO–ZnS electron transport layer, *J. Am. Chem. Soc.*, 2019, **141**, 541–547.

4 J. Liu, Q. Zhou, N. K. Thein, L. Tian, D. Jia, E. M. J. Johansson and X. Zhang, In situ growth of perovskite stacking layers for high-efficiency carbon-based hole conductor free perovskite solar cells, *J. Mater. Chem. A*, 2019, **7**, 13777–13786.

5 B. Liu, M. Long, M. Cai, L. Ding and J. Yang, Interfacial charge behavior modulation in 2D/3D perovskite heterostructure for potential high-performance solar cells, *Nano Energy*, 2019, **59**, 715–720.

6 X. Qiu, Y. Liu, W. Li and Y. Hu, Traps in metal halide perovskites: characterization and passivation, *Nanoscale*, 2020, **12**, 22425–22451.

7 A. Kojima, K. Teshima, Y. Shirai and T. Miyasaka, Organometal halide perovskites as visible-light sensitizers for photovoltaic cells, *J. Am. Chem. Soc.*, 2009, **131**, 6050–6051.

8 H.-S. Kim, C.-R. Lee, J.-H. Im, K.-B. Lee, T. Moehl, A. Marchioro, S.-J. Moon, R. Humphry-Baker, J.-H. Yum, J. E. Moser, M. Grätzel and N.-G. Park, Lead iodide perovskite sensitized all-solid-state submicron thin film mesoscopic solar cell with efficiency exceeding 9%, *Sci. Rep.*, 2012, **2**, 591.

9 Q. Jiang, Y. Zhao, X. Zhang, X. Yang, Y. Chen, Z. Chu, Q. Ye, X. Li, Z. Yin and J. You, Surface passivation of perovskite film for efficient solar cells, *Nat. Photonics*, 2019, **13**, 460–466.

10 X. Zhou, M. Hu, C. Liu, L. Zhang, X. Zhong, X. Li, Y. Tian, C. Cheng and B. Xu, Synergistic effects of multiple functional ionic liquid-treated PEDOT:PSS and less-ion-defects S-acetylthiocholine chloride-passivated perovskite surface enabling stable and hysteresis-free inverted perovskite solar cells with conversion efficiency over 20%, *Nano Energy*, 2019, **63**, 103866.

11 W. Kong, W. Li, C. Liu, H. Liu, J. Miao, W. Wang, S. Chen, M. Hu, D. Li, A. Amini, S. Yang, J. Wang, B. Xu and C. Cheng, Organic monomolecular layers enable energy-level matching for efficient hole transporting layer free inverted perovskite solar cells, *ACS Nano*, 2019, **13**, 1625–1634.

12 G. Sathiyan, A. A. Syed, C. Chen, C. Wu, L. Tao, X. Ding, Y. Miao, G. Li, M. Cheng and L. Ding, Dual effective dopant based hole transport layer for stable and efficient perovskite solar cells, *Nano Energy*, 2020, **72**, 104673.

13 M. Hu, L. Zhang, S. She, J. Wu, X. Zhou, X. Li, D. Wang, J. Miao, G. Mi, H. Chen, Y. Tian, B. Xu and C. Cheng, Electron transporting bilayer of SnO_2 and TiO_2 nanocolloid enables highly efficient planar perovskite solar cells, *Sol. RRL*, 2020, **4**, 1900331.

14 D. Li, C. Liu, S. Chen, W. Kong, H. Zhang, D. Wang, Y. Li, J. Chang and C. Cheng, Simplified compact perovskite

solar cells with efficiency of 19.6% via interface engineering, *Energy Environ. Mater.*, 2020, **3**, 5–11.

15 *Best Research-Cell Efficiencies Chart*, https://www.nrel.gov/pv/cell-efficiency.html, accessed 11 March, 2021.

16 R. Wang, J. Xue, K.-L. Wang, Z.-K. Wang, Y. Luo, D. Fenning, G. Xu, S. Nuryyeva, T. Huang, Y. Zhao, J. L. Yang, J. Zhu, M. Wang, S. Tan, I. Yavuz, K. N. Houk and Y. Yang, Constructive molecular configurations for surface-defect passivation of perovskite photovoltaics, *Science*, 2019, **366**, 1509.

17 Z. Li, C. Xiao, Y. Yang, S. P. Harvey, D. H. Kim, J. A. Christians, M. Yang, P. Schulz, S. U. Nanayakkara, C.-S. Jiang, J. M. Luther, J. J. Berry, M. C. Beard, M. M. Al-Jassim and K. Zhu, Extrinsic ion migration in perovskite solar cells, *Energy Environ. Sci.*, 2017, **10**, 1234–1242.

18 A. Kogo and M. Chikamatsu, Cesium iodide post-treatment of organic–inorganic perovskite crystals to improve photovoltaic performance and thermal stability, *Nanoscale*, 2020, **12**, 21605–21609.

19 C. Li, J. Yin, R. Chen, X. Lv, X. Feng, Y. Wu and J. Cao, Monoammonium porphyrin for blade-coating stable large-area perovskite solar cells with >18% efficiency, *J. Am. Chem. Soc.*, 2019, **141**, 6345–6351.

20 J. Cao, C. Li, X. Lv, X. Feng, R. Meng, Y. Wu and Y. Tang, Efficient grain boundary suture by low-cost tetra-ammonium zinc phthalocyanine for stable perovskite solar cells with expanded photoresponse, *J. Am. Chem. Soc.*, 2018, **140**, 11577–11580.

21 J. Yang, Q. Bao, L. Shen and L. Ding, Potential applications for perovskite solar cells in space, *Nano Energy*, 2020, **76**, 105019.

22 C. Zuo, H. J. Bolink, H. Han, J. Huang, D. Cahen and L. Ding, Advances in perovskite solar cells, *Adv. Sci.*, 2016, **3**, 1500324.

23 M. Yang, T. Zhang, P. Schulz, Z. Li, G. Li, D. H. Kim, N. Guo, J. J. Berry, K. Zhu and Y. Zhao, Facile fabrication of large-grain $CH_3NH_3PbI_{3-x}Br_x$ films for high-efficiency solar cells via CH_3NH_3Br-selective Ostwald ripening, *Nat. Commun.*, 2016, **7**, 12305.

24 D.-Y. Son, J.-W. Lee, Y. J. Choi, I.-H. Jang, S. Lee, P. J. Yoo, H. Shin, N. Ahn, M. Choi, D. Kim and N.-G. Park, Self-formed grain boundary healing layer for highly efficient $CH_3NH_3PbI_3$ perovskite solar cells, *Nat. Energy*, 2016, **1**, 16081.

25 X. Zhang, J. Zhang, D. Phuyal, J. Du, L. Tian, V. A. Öberg, M. B. Johansson, U. B. Cappel, O. Karis, J. Liu, H. Rensmo, G. Boschloo and E. M. J. Johansson, Inorganic $CsPbI_3$ perovskite coating on PbS quantum dot for highly efficient and stable infrared light converting solar cells, *Adv. Energy Mater.*, 2018, **8**, 1702049.

26 N. Li, S. Tao, Y. Chen, X. Niu, C. K. Onwudinanti, C. Hu, Z. Qiu, Z. Xu, G. Zheng, L. Wang, Y. Zhang, L. Li, H. Liu, Y. Lun, J. Hong, X. Wang, Y. Liu, H. Xie, Y. Gao, Y. Bai, S. Yang, G. Brocks, Q. Chen and H. Zhou, Cation and anion immobilization through chemical bonding enhancement with fluorides for stable halide perovskite solar cells, *Nat. Energy*, 2019, **4**, 408–415.

27 J.-H. Cha, K. Noh, W. Yin, Y. Lee, Y. Park, T. K. Ahn, A. Mayoral, J. Kim, D.-Y. Jung and O. Terasaki, Formation and encapsulation of all-Inorganic lead halide perovskites at room temperature in metal–organic frameworks, *J. Phys. Chem. Lett.*, 2019, **10**, 2270–2277.

28 Y. Wang, Z. Zhang, M. Tao, Y. Lan, M. Li, Y. Tian and Y. Song, Interfacial modification towards highly efficient and stable perovskite solar cells, *Nanoscale*, 2020, **12**, 18563–18575.

29 Y. Liu, S. Akin, L. Pan, R. Uchida, N. Arora, J. V. Milić, A. Hinderhofer, F. Schreiber, A. R. Uhl, S. M. Zakeeruddin, A. Hagfeldt, M. I. Dar and M. Grätzel, Ultrahydrophobic 3D/2D fluoroarene bilayer-based water-resistant perovskite solar cells with efficiencies exceeding 22%, *Sci. Adv.*, 2019, **5**, eaaw2543.

30 Q. Yao, Q. Xue, Z. Li, K. Zhang, T. Zhang, N. Li, S. Yang, C. J. Brabec, H.-L. Yip and Y. Cao, Graded 2D/3D perovskite heterostructure for efficient and operationally stable MA-Free perovskite solar cells, *Adv. Mater.*, 2020, **32**, 2000571.

31 Y.-W. Jang, S. Lee, K. M. Yeom, K. Jeong, K. Choi, M. Choi and J. H. Noh, Intact 2D/3D halide junction perovskite solar cells via solid-phase in-plane growth, *Nat. Energy*, 2021, **6**, 63–71.

32 Z. Ji, H. Wang, S. Canossa, S. Wuttke and O. M. Yaghi, Pore chemistry of metal–organic frameworks, *Adv. Funct. Mater.*, 2020, **30**, 2000238.

33 Y. Ye, L. Gong, S. Xiang, Z. Zhang and B. Chen, Metal–organic frameworks as a versatile platform for proton conductors, *Adv. Mater.*, 2020, **32**, 1907090.

34 D. Shen, A. Pang, Y. Li, J. Dou and M. Wei, Metal–organic frameworks at interfaces of hybrid perovskite solar cells for enhanced photovoltaic properties, *Chem. Commun.*, 2018, **54**, 1253–1256.

35 A. J. Huckaba, D. T. Sun, A. A. Sutanto, M. Mensi, Y. Zhang, W. L. Queen and M. K. Nazeeruddin, Lead sequestration from perovskite solar cells using a metal–organic framework polymer composite, *Energy Technol.*, 2020, **8**, 2000239.

36 X. Zhou, L. Qiu, R. Fan, J. Zhang, S. Hao and Y. Yang, Heterojunction incorporating perovskite and microporous metal–organic framework nanocrystals for efficient and stable solar cells, *Nano-Micro Lett.*, 2020, **12**, 2–11.

37 J. Zhang, S. Guo, M. Zhu, C. Li, J. Chen, L. Liu, S. Xiang and Z. Zhang, Simultaneous defect passivation and hole mobility enhancement of perovskite solar cells by incorporating anionic metal-organic framework into hole transport materials, *Chem. Eng. J.*, 2020, **408**, 127328.

38 Y. Dong, J. Zhang, Y. Yang, L. Qiu, D. Xia, K. Lin, J. Wang, X. Fan and R. Fan, Self-assembly of hybrid oxidant POM@Cu-BTC for enhanced efficiency and long-term stability of perovskite solar cells, *Angew. Chem., Int. Ed.*, 2019, **58**, 17610–17615.

39 M. Li, J. Wang, A. Jiang, D. Xia, X. Du, Y. Dong, P. Wang, R. Fan and Y. Yang, Metal organic framework doped Spiro-OMeTAD with increased conductivity for improving

perovskite solar cell performance, *Sol. Energy*, 2019, **188**, 380–385.

40 M. Li, D. Xia, Y. Yang, X. Du, G. Dong, A. Jiang and R. Fan, Doping of $[In_2(phen)_3Cl_6]\cdot CH_3CN\cdot 2H_2O$ indium-based metal–organic framework into hole transport layer for enhancing perovskite solar cell efficiencies, *Adv. Energy Mater.*, 2018, **8**, 1702052.

41 T. M. H. Nguyen and C. W. Bark, Synthesis of cobalt-doped TiO_2 based on metal–organic frameworks as an effective electron transport material in perovskite solar cells, *ACS Omega*, 2020, **5**, 2280–2286.

42 T.-H. Chang, C.-W. Kung, H.-W. Chen, T.-Y. Huang, S.-Y. Kao, H.-C. Lu, M.-H. Lee, K. M. Boopathi, C.-W. Chu and K.-C. Ho, Planar heterojunction perovskite solar cells incorporating metal–organic framework nanocrystals, *Adv. Mater.*, 2015, **27**, 7229–7235.

43 U. Ryu, S. Jee, J.-S. Park, I. K. Han, J. H. Lee, M. Park and K. M. Choi, Nanocrystalline titanium metal–organic frameworks for highly efficient and flexible perovskite solar cells, *ACS Nano*, 2018, **12**, 4968–4975.

44 C.-C. Lee, C.-I. Chen, Y. T. Liao, K. C.-W. Wu and C. C. Chueh, Enhancing efficiency and stability of photovoltaic cells by using perovskite/Zr-MOF heterojunction including bilayer and hybrid structures, *Adv. Sci.*, 2019, **6**, 1801715.

45 S. Wu, Z. Li, M.-Q. Li, Y. Diao, F. Lin, T. Liu, J. Zhang, P. Tieu, W. Gao, F. Qi, X. Pan, Z. Xu, Z. Zhu and A. K. Y. Jen, 2D metal–organic framework for stable perovskite solar cells with minimized lead leakage, *Nat. Nanotechnol.*, 2020, **15**, 934–940.

46 J. Sánchez-Laínez, B. Zornoza, S. Friebe, J. Caro, S. Cao, A. Sabetghadam, B. Seoane, J. Gascon, F. Kapteijn, C. Le Guillouzer, G. Clet, M. Daturi, C. Téllez and J. Coronas, Influence of ZIF-8 particle size in the performance of polybenzimidazole mixed matrix membranes for pre-combustion CO_2 capture and its validation through interlaboratory test, *J. Membr. Sci.*, 2016, **515**, 45–53.

47 H. Lu, Y. Liu, P. Ahlawat, A. Mishra, W. R. Tress, F. T. Eickemeyer, Y. Yang, F. Fu, Z. Wang, C. E. Avalos, B. I. Carlsen, A. Agarwalla, X. Zhang, X. Li, Y. Zhan, S. M. Zakeeruddin, L. Emsley, U. Rothlisberger, L. Zheng, A. Hagfeldt and M. Grätzel, Vapor-assisted deposition of highly efficient, stable black-phase $FAPbI_3$ perovskite solar cells, *Science*, 2020, **370**, eabb8985.

48 J.-W. Lee, Z. Dai, C. Lee, H. M. Lee, T.-H. Han, N. De Marco, O. Lin, C. S. Choi, B. Dunn, J. Koh, D. Di Carlo, J. H. Ko, H. D. Maynard and Y. Yang, Tuning molecular interactions for highly reproducible and efficient formamidinium perovskite solar cells via adduct approach, *J. Am. Chem. Soc.*, 2018, **140**, 6317–6324.

49 D. Bi, X. Li, J. V. Milić, D. J. Kubicki, N. Pellet, J. Luo, T. LaGrange, P. Mettraux, L. Emsley, S. M. Zakeeruddin and M. Grätzel, Multifunctional molecular modulators for perovskite solar cells with over 20% efficiency and high operational stability, *Nat. Commun.*, 2018, **9**, 4482.

50 Y. Cheng, X. Liu, Z. Guan, M. Li, Z. Zeng, H.-W. Li, S.-W. Tsang, A. G. Aberle and F. Lin, Revealing the degradation and self-healing mechanisms in perovskite solar cells by sub-bandgap external quantum efficiency spectroscopy, *Adv. Mater.*, 2021, **33**, 2006170.